Human BPAG1-r:5′- TGGCAGAGCTGTAAGATCCA-3′
Human BPAG2-f:5′- GCTGGAGATCTGGATTACAATGA-3′
Human BPAG2-r:5′- CCTTGCAGTAGGCCCTGA-3′
Human β-actin -f:5′- GAGCTACGAGCTGCCTGACG-3′
Human β-actin -r:5′- GTAGTTTCGTGGATGCCACAG-3′

Detection of BPAG1 by Immunoprecipitation (IP) and Western blotting

Cells (1×10^7) were trypsinized, washed in cold PBS and resuspended in 500 µl RIPA buffer. IP of total cell lysates were incubated with anti-BPAG1 antibody (sc-13776) (Santa Cruz Biotechnology Inc., USA) or normal goat IgG (Santa Cruz) for 1 h followed by protein G agarose (GE Healthcare) overnight. SDS-PAGE and Western blotting were performed, as previously described [16] with anti-BPAG1 antibody. After incubation with HRP conjugated anti-goat IgG (R&D systems, USA), signals were detected with ECL Western Blotting Detection Regents (GE Healthcare) according to the manufacturer's instructions.

Quantification of BPAG1 auto-antibodies in sera

Approval for this study was obtained from the Institutional Review Board of the Osaka University Hospital (#08312). Written informed consent was obtained from all participants before the study. We collected sera from 55 melanoma patients and 27 healthy volunteers. The malignant melanoma patients studied here consisted of 24 men and 31 women with an average age of 62.6 years (range, 22 to 86 years); 13 had stage 0 (*in situ*) or stage I; 5 had stage II; 11 had stage III; 26 had stage IV. The healthy volunteers consisted of 15 men and 12 women with an average age of 31.6 years (range, 24 to 49years). The sera samples were stored at −30°C prior to use and the serum levels of anti-BPAG1 auto-antibodies were determined using a BP230 ELISA kit (MBL, Japan) according to the manufacturer's instructions. The INDEX was calculated as follows; INDEX = (sample absorbance − negative control absorbance [INDEX = 0])/(positive control absorbance [INDEX = 100] - negative control absorbance) ×100 [17]. The Mann-Whitney U test was used to determine statistical significance, and $p<0.05$ was considered statistically significant.

Results

Identification of bpag1 as a tumor antigen recognized by auto-antibodies

An overview of the screening procedure is shown in Figure 1. We performed the screening on mouse F10 melanoma cell lines. The tumor-homing phages were collected by *in vivo* biopanning in tumor-bearing mice. The phages were used to infect HB2151 for scFv expression and plated on a 2×YT agar plate. After 16 h, scFv expression was induced with IPTG, and the resulting scFvs were transferred onto a nitrocellulose membrane. The membrane was incubated with F10 melanoma tumor lysate followed by F10 tumor-bearing mouse serum. The scFv-tumor protein complexes on the nitrocellulose membrane were detected with the auto-antibodies in the serum collected from the tumor-bearing mice (Figure 2A). We performed the screening procedure several times and selected high-signal clones, distinct from background signals, for further experiments. Next, we analyzed the proteins that were detected with auto-antibodies by performing MALDI-TOF mass spectrometry, and we identified 8 potential melanoma marker candidates with statistical significance ($p<0.05$) (Figure 2B). The candidates were ordered according to the expectation value, which is the expected frequency of the matches to be obtained from mass spectrometry merely by chance. We compared the expression of the 8 candidates among NIH-3T3 cells, F10 melanoma cells and F10 melanoma tumors by real-time PCR. Bpag1, tbc1d13 and c7orf30 were expressed at much higher levels in F10 melanoma cells (7.0-, 3.1- and 1.9-fold, respectively) and F10 melanoma tumors (10.9-, 4.2- and 6.3-fold, respectively) as compared to NIH-3T3 cells (Figure 2C); the expression levels of the remaining 5 candidates in melanoma cells and tumors were less than the expression level in NIH-3T3 cells (data not shown). Among the three candidates, we selected bpag1 for further investigation because bpag1 was expressed most abundantly in F10 melanoma cells and tumors, and is known to have a restricted tissue expression pattern, including skin, brain and muscle [18].

Differential expression of BPAG1 and BPAG2 in normal human melanocytes and human melanoma cell lines

We used RT-PCR to confirm the expression of BPAG1 in human melanomas. BPAG1 is expressed in normal human keratinocytes and is a component of hemidesmosomes along with BPAG2. Thus, we used normal human keratinocytes as a positive control for both these proteins. We identified BPAG1 expression in human melanoma cell lines (A375 and G361) and normal human melanocytes (Figure 3A). However, we did not detect BPAG2 expression in the human melanoma cell lines or normal human melanocytes (Figure 3A). We also detected BPAG1 protein in A375 and G361 by IP-western blotting (Figure 3B).

Quantification of anti-BPAG1 auto-antibodies in sera

Auto-antibodies against BPAG1 are found in sera from BP and therefore BPAG1 maybe a highly immunogenic protein. We hypothesized that the human immune system might generate auto-antibodies against BPAG1 expressed in human melanomas. To assess this possibility, we collected sera from 55 melanoma patients and 27 healthy volunteers and quantified the serum levels of anti-BPAG1 auto-antibodies by ELISA (Figure 4A). The average (±S.E.M.) INDEX value of the control group and the melanoma group was 1.64 (±0.27) and 3.47 (±0.40), respectively. We classified melanoma patients as follows: *in situ*, stage I or stage II patients were "early" (n = 18), and stage III or stage IV patients were "advanced" (n = 37). The levels of anti-BPAG1 auto-antibodies were much higher in both early and advanced stage melanoma patients ($p<0.01$) as compared to the healthy volunteers (Figure 4B). The average INDEX value (±S.E.M.) for the early and advanced melanoma patients was 4.14 (±0.83) and 3.15 (±0.43), respectively. Next, we evaluated the possibility of using anti-BPAG1 auto-antibodies as a melanoma detection marker. The maximum INDEX value in healthy volunteers (4.64) was defined as the cut off level. Applying these criteria, the positive rates of serum anti-BPAG1 auto-antibodies were 23.6% in total melanoma patients (13/55), 33.3% in early stage melanoma patients (6/18), and 18.9% in advanced stage melanoma patients (7/37) (Table 1). We also conducted indirect immunofluorescence studies using 4 melanoma patients' sera and demonstrated that IgG antibodies produced in patients reacted with skin basement membrane zone with variability in staining intensive (down to a dilution of 1:160).

Discussion

In the present study, we developed a novel screening method for detecting tumor biomarkers. Our method is similar to SEREX in that we use serum containing anti-tumor auto-antibodies, but unlike SEREX, however, our method does not require a cDNA library from tumor tissue [19,20,21]. We anticipate that our method has clinical applicability, because it can be applied to human patients by modifying the method to select tumor-homing

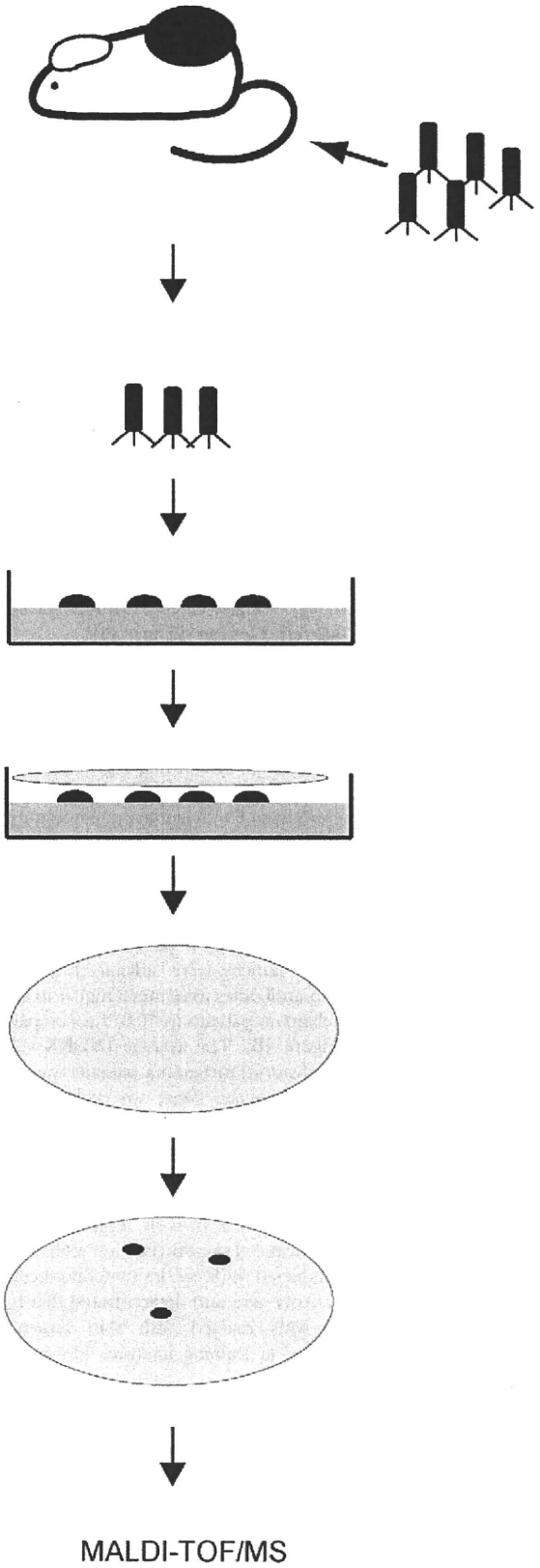

Figure 1. Overview of the rapid method for isolating auto-antibody against tumor-associated antigen (TAA) using a scFv library. The tumor-homing scFv-presenting phages were collected from tumors that were injected with a scFv library. The collected phages were infected to

HB2151 for scFv secretion. The secreted scFvs from HB2151 were transferred to nitrocellulose membranes by colony lift. The membranes were incubated with tumor lysate followed by serum from a tumor-bearing mouse. The scFv-tumor protein complex was detected by auto-antibodies. The complex was digested into peptide by trypsin and analyzed using MALDI-TOF mass spectrometry for identification.
doi:10.1371/journal.pone.0010566.g001

phage. In this report, we selected tumor-homing phage using tumor-bearing mice, but it is also possible to use tumor specimens [22]. Moreover, the phage screening could be conducted in human cancer patients without any detectable toxicity [23]. This method therefore has the potential to identify the most suitable tumor antigens for diagnosis or vaccination.

Nevertheless, our method did not detect previously identified melanoma antigens, such as gp100, tyrosinase, TRP-1 and TRP-2; instead, it detected completely different proteins. Gp100, tyrosinase, and TRP-2 were identified previously as melanoma antigens recognized by cytotoxic T cells from cancer patients, and TRP-1 was identified as a melanoma antigen recognized by IgG antibodies in the serum of a melanoma patient [24]. The epitopes of these antigens can efficiently activate tumor immunity, and they have been developed for cancer immunotherapy trials [25]. Although auto-antibodies to these melanoma antigens were detected in the sera of melanoma patients, the antigens were not frequently identified in sera from melanoma patients [26,27,28]. A possible explanation might be that auto-antibodies to such melanoma antigens exist in the sera of melanoma patients, but lack sensitivity or are present at low titers. Proteins identified by our screening method, however, have the potential to elicit the production of auto-antibodies in tumor-bearing individuals. In other words, our screening method may detect highly immunogenic proteins. Thus, it can be an effective tool for identifying detection markers in serum.

Given the differences in immune systems between mice and human, it is possible that the positive results screened in mice might

A

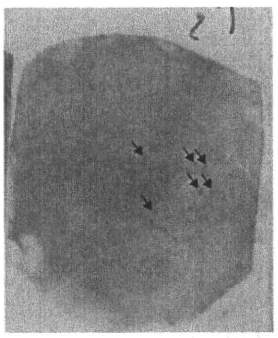

B

protein	expect
Diamine acetyltransferase 2 (sat2)	0.0021
Bullous pemphigoid antigen 1, isoforms1/2/3/4 (bpag1)	0.0036
voltage-dependent calcium channel subunit alpha2/delta3 (cacna2d3)	0.028
LRR and PYD domains-containing protein F4 (nal4f)	0.038
TBC1 domain family member 13 (tbc1d13)	0.04
nibrin	0.04
Uncharacterized protein C7orf30 homolog (c7orf30)	0.045
serine/threonine-protein kinase (plk2)	0.047

C

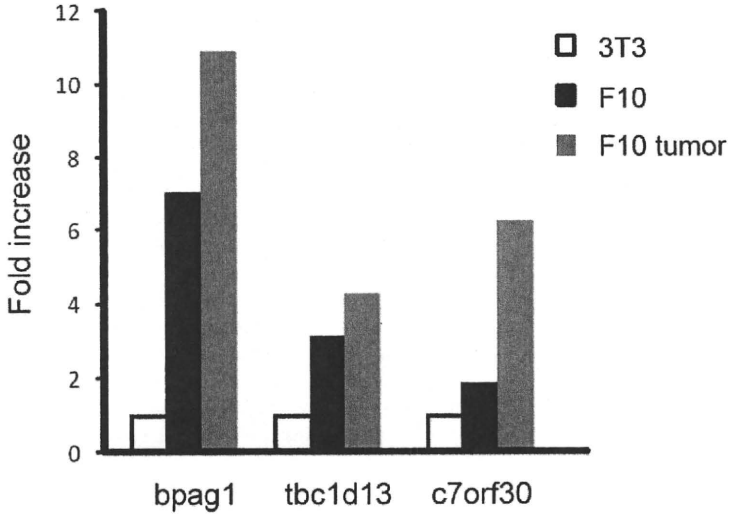

Figure 2. Identification of bpag1 as a tumor antigen recognized by auto-antibodies. (A) An example of the screening output. ScFv-tumor antigen complex was detected with auto-antibodies in tumor-bearing mouse serum. (B) Eight candidates were identified by MALDI-TOF mass spectrometry with statistical significance ($p<0.05$); expect = expectation value. (C) Comparison of bpag1, tbc1d13 and c7orf30 expression in NIH-3T3 cells (white bar), F10 melanoma cells (black bar) and F10 melanoma tumors (grey bar) by SYBR Green real-time PCR.
doi:10.1371/journal.pone.0010566.g002

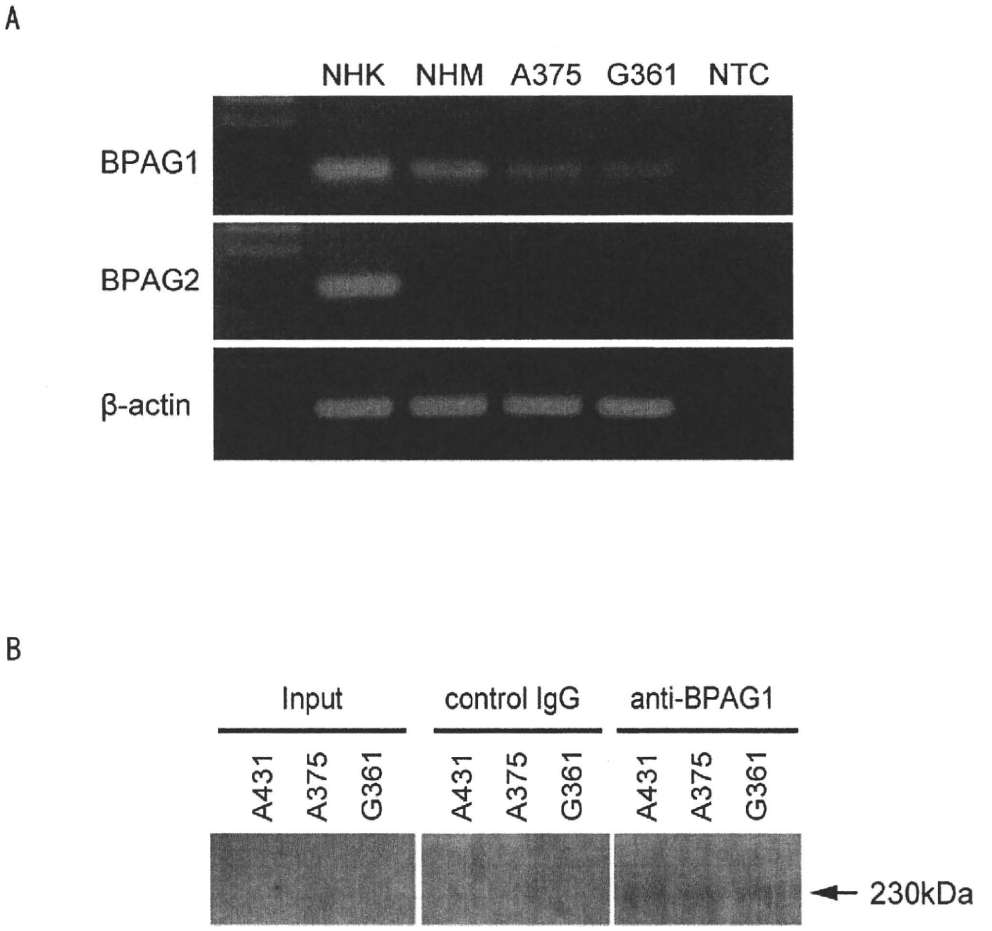

Figure 3. Expression of BPAG1 in normal human melanocytes and human melanoma cell lines. (A) The expression of BPAG1 and BPAG2 mRNA was quantified by RT-PCR in normal human melanocytes (NHM) and human melanoma cell lines A375 and G361. Normal human keratinocyte (NHK) mRNA was used as a positive control. β-actin was amplified as a loading control for cDNA. NTC; no template control. (B) The expression of BPAG1 protein was detected by IP-western blotting in human melanoma cell lines A375 and G361. A431 was used as positive control for BPAG1. The arrow indicates BPAG1.
doi:10.1371/journal.pone.0010566.g003

be negative in humans. Ideally, screening procedures for auto-antibodies need to be performed in human melanoma patients. However, although the phage screening has been conducted in human cancer patients without any detectable toxicity, the method is still at a clinical trial stage [23]. It is therefore not yet straightforward or practicable to conduct phage screening in humans. With regards to our studies, screening mice also has the advantages of repeatability and uniformity of samples. On the other hand, it is difficult to conduct repeated screening in human cancer patients. Moreover, since the background of all the murine samples is uniform in our screening, any consistently positive result from repeated screenings will be highly reliable as tumor markers. In contrast, since the tumor stages and immunological states of patients are diverse, the results of screening using human patient sera would need extensive re-validation work.

We also showed that BPAG1 is expressed in human melanoma cell lines and that auto-antibodies against BPAG1 can be a potent melanoma marker. BPAG1 is expressed in normal keratinocytes within hemidesmosomes in association with BPAG2 and other proteins [8]. We did not detect any BPAG2 expression in human melanoma cell lines and melanocytes, and thus BPAG1 may have distinct functions in melanomas and melanocytes. BPAG1 is also expressed in some neurons and is involved in axonal neurofilament aggregation and axonal microtubule disorganization [29,30]. The expression of BPAG1 in a human epidermoid carcinoma cell line (A431) and mammary ductal carcinoma *in situ* has also been confirmed [31,32]. Thus BPAG1 may have an as yet undefined role related to tumorigenesis or tumor progression; overexpression and suppression of BPAG1 in melanocytes and melanomas will be necessary to determine this in more detail.

Some patients with melanoma develop vitiligo-like white patches, known as melanoma-associated hypopigmentation (MAH), on their skin [33]. Interestingly, the presence of vitiligo in melanoma patients may correlate with improved prognosis [34,35]. Such patients with vitiligo could have more effective immunity against melanoma than patients without vitiligo. In general, the appearance of autoimmune phenomena improves the outcome of cancer patients [36]. However, such autoimmune phenomena are suppressed in most cancer patients by regulatory T (Treg) cells [37]. Treg cells inhibit $CD8^+$ and $CD4^+$ T cells, which are major components of cancer immunosuppression [38,39]. The depletion of Treg cells from tumor-bearing mice promotes tumor regression [38,39]. Interestingly, auto-antibodies

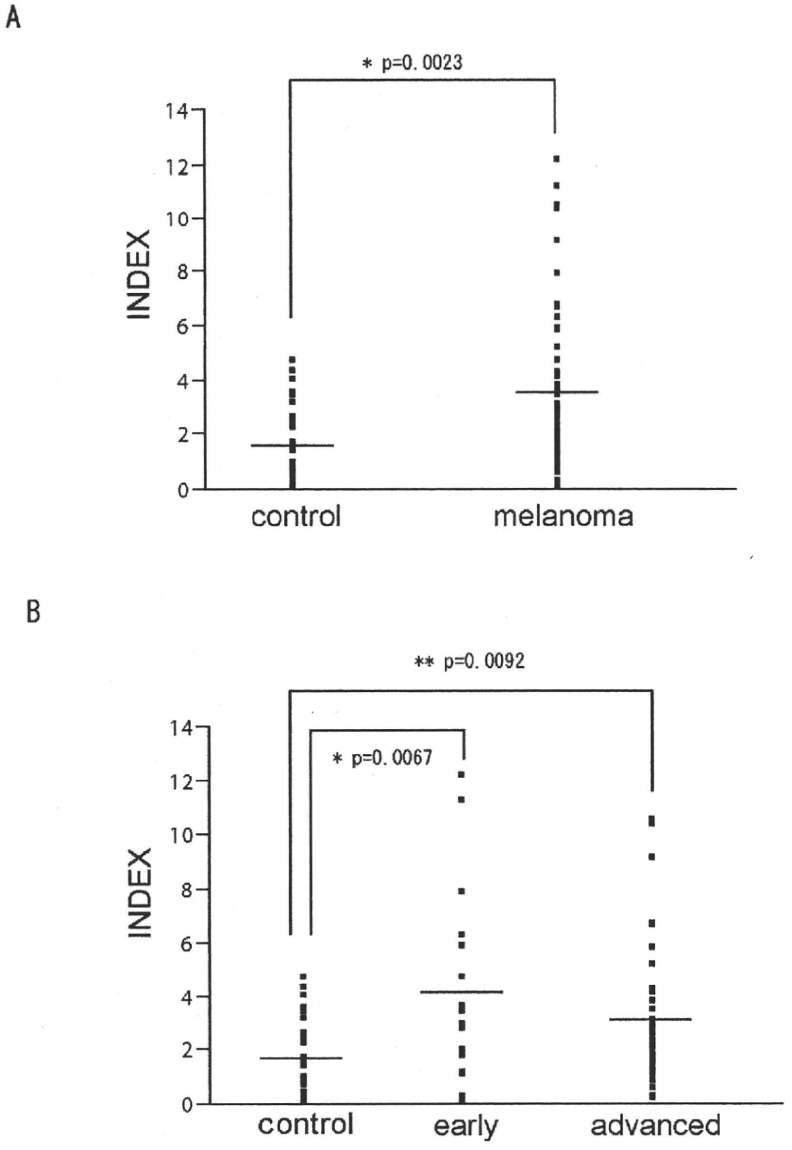

Figure 4. Quantification of anti-BPAG1 auto-antibodies in melanoma patients. (A) The levels of anti-BPAG1 auto-antibodies in sera collected from healthy volunteers and melanoma patients were quantified using a MESACUP BP230 ELISA Kit. The INDEX values were plotted and the average INDEX values as shown (±S.E.M.) for control subjects (1.64±0.27) and melanoma patients (3.47±0.40). (B) The melanoma patients were classified using the American Joint Committee on Cancer (AJCC) 2002 staging criteria. *In situ*, stage I or stage II patients were categorized as "early", while stage III or stage IV patients were categorized as "advanced". The average INDEX values (±S.E.M.) of early and advanced melanoma patients were 4.14±0.83 and 3.15±0.43, respectively; the bars indicate the average INDEX value.
doi:10.1371/journal.pone.0010566.g004

were detected in mice showing tumor regression [38]. The efficiency of Treg-cell depletion may correlate with the emergence of auto-antibodies. Thus, the presence of anti-BPAG1 auto-antibodies may correlate with the occurrence of autoimmune responses in melanoma patients. By quantification of anti-BPAG1 auto-antibodies, it maybe possible to predict the immune status of cancer patients. In theory, immunotherapy against melanoma, therefore, might be more effective for patients with anti-BPAG1 auto-antibodies than those without antibodies.

We showed that BPAG1 is expressed both in melanocytes and melanomas. Since BPAG1 expression is maintained throughout the stages of melanoma tumorigenesis, BPAG1 auto-antibodies can be created even in the early stage of melanoma. We showed that the levels of anti-BPAG1 auto-antibodies are higher in melanoma patients at both early and advanced stages than in healthy volunteers (Figure 4 and Table 1). This result suggests that anti-BPAG1 auto-antibodies can be present in early stage melanoma, i.e. before it metastasizes. Thus, anti-BPAG1 auto-antibodies have the potential to be a promising melanoma biomarker. To test this hypothesis, we are planning to conduct a larger clinical study.

To the best of our knowledge, this report is the first to show BPAG1 expression in human melanomas and melanocytes and to highlight the potential of anti-BPAG1 auto-antibodies in the serum

Table 1. Positive rates of serum anti-BPAG1 auto-antibody in stage-classified melanoma patients.

stage	total sample number	BPAG1 auto-antibody positive	%
early	18	6	33.3
advanced	37	7	18.9
total	55	13	23.6

The maximum INDEX value in healthy volunteers (4.64) was defined as the cut off level. The patients were classified by using the American Joint Committee on Cancer (AJCC) 2002 staging criteria. *In situ*, stage I or stage II patients were classified as "early", while stage III or stage IV patients were classified as "advanced".
doi:10.1371/journal.pone.0010566.t001

.as a marker of melanoma. We also demonstrated the effectiveness of our screening method. We will continue to develop this method into a more sophisticated method that can be used clinically. To validate the use of anti-BPAG1 auto-antibodies for melanoma diagnosis, we need to clarify the function of BPAG1 in melanoma and the mechanism of auto-antibody creation. These studies will be fundamental in assessing whether BPAG1 auto-antibodies can have an impact on improving the prognosis of melanomas.

Author Contributions

Conceived and designed the experiments: TS YK. Performed the experiments: TS. Analyzed the data: TS AT KT. Contributed reagents/materials/analysis tools: AT TY IK. Wrote the paper: TS YK.

References

1. Jemal A, Siegel R, Ward E, Hao Y, Xu J, et al. (2008) Cancer statistics, 2008. CA Cancer J Clin 58: 71–96.
2. Bosserhoff AK (2006) Novel biomarkers in malignant melanoma. Clin Chim Acta 367: 28–35.
3. Gould Rothberg BE, Bracken MB, Rimm DL (2009) Tissue biomarkers for prognosis in cutaneous melanoma: a systematic review and meta-analysis. J Natl Cancer Inst 101: 452–474.
4. Ohsie SJ, Sarantopoulos GP, Cochran AJ, Binder SW (2008) Immunohistochemical characteristics of melanoma. J Cutan Pathol 35: 433–444.
5. Brochez L, Naeyaert JM (2000) Serological markers for melanoma. Br J Dermatol 143: 256–268.
6. Ikuta Y, Nakatsura T, Kageshita T, Fukushima S, Ito S, et al. (2005) Highly sensitive detection of melanoma at an early stage based on the increased serum secreted protein acidic and rich in cysteine and glypican-3 levels. Clin Cancer Res 11: 8079–8088.
7. Nakatsura T, Kageshita T, Ito S, Wakamatsu K, Monji M, et al. (2004) Identification of glypican-3 as a novel tumor marker for melanoma. Clin Cancer Res 10: 6612–6621.
8. Kasperkiewicz M, Zillikens D (2007) The pathophysiology of bullous pemphigoid. Clin Rev Allergy Immunol 33: 67–77.
9. Guo L, Degenstein L, Dowling J, Yu QC, Wollmann R, et al. (1995) Gene targeting of BPAG1: abnormalities in mechanical strength and cell migration in stratified epithelia and neurologic degeneration. Cell 81: 233–244.
10. Labib RS, Anhalt GJ, Patel HP, Mutasim DF, Diaz LA (1986) Molecular heterogeneity of the bullous pemphigoid antigens as detected by immunoblotting. J Immunol 136: 1231–1235.
11. Mutasim DF, Takahashi Y, Labib RS, Anhalt GJ, Patel HP, et al. (1985) A pool of bullous pemphigoid antigen (s) is intracellular and associated with the basal cell cytoskeleton-hemidesmosome complex. J Invest Dermatol 84: 47–53.
12. Stanley JR, Hawley-Nelson P, Yuspa SH, Shevach EM, Katz SI (1981) Characterization of bullous pemphigoid antigen: a unique basement membrane protein of stratified squamous epithelia. Cell 24: 897–903.
13. Liu Z, Diaz LA, Troy JL, Taylor AF, Emery DJ, et al. (1993) A passive transfer model of the organ-specific autoimmune disease, bullous pemphigoid, using antibodies generated against the hemidesmosomal antigen, BP180. J Clin Invest 92: 2480–2488.
14. de Wildt RMT, Mundy CR, Gorick BD, Tomlinson IM (2000) Antibody arrays for high-throughput screening of antibody-antigen interactions. Nat Biotechnol 18: 989–994.
15. Lee L, Garrood T, Pitzalis C (2007) In vivo phage display selection in the human/SCID mouse chimera model for defining synovial specific determinants. Methods Mol Med 136: 369–394.
16. Tanaka M, Shimbo T, Kikuchi Y, Matsuda M, Kaneda Y (2010) Sterile alpha motif containing domain 9 is involved in death signaling of malignant glioma treated with inactivated Sendai virus particle (HVJ-E) or type I interferon. Int J Cancer 126: 1982–1991.
17. Nishie W, Sawamura D, Goto M, Ito K, Shibaki A, et al. (2007) Humanization of autoantigen. Nat Med 13: 378–383.
18. Okumura M, Yamakawa H, Ohara O, Owaribe K (2002) Novel alternative splicings of BPAG1 (bullous pemphigoid antigen 1) including the domain structure closely related to MACF (microtubule actin cross-linking factor). J Biol Chem 277: 6682–6687.
19. Sahin U, Tureci O, Schmitt H, Cochlovius B, Johannes T, et al. (1995) Human neoplasms elicit multiple specific immune responses in the autologous host. Proc Natl Acad Sci U S A 92: 11810–11813.
20. Li G, Miles A, Line A, Rees RC (2004) Identification of tumour antigens by serological analysis of cDNA expression cloning. Cancer Immunol Immunother 53: 139–143.
21. Gunawardana CG, Diamandis EP (2007) High throughput proteomic strategies for identifying tumour-associated antigens. Cancer Lett 249: 110–119.
22. Sun Y, Shukla GS, Weaver D, Pero SC, Krag DN (2009) Phage-display selection on tumor histological specimens with laser capture microdissection. J Immunol Methods 347: 46–53.
23. Krag DN, Shukla GS, Shen GP, Pero S, Ashikaga T, et al. (2006) Selection of tumor-binding ligands in cancer patients with phage display libraries. Cancer Res 66: 7724–7733.
24. Kawakami Y, Rosenberg SA (1997) Human tumor antigens recognized by T-cells. Immunol Res 16: 313–339.
25. Rosenberg SA, Yang JC, Restifo NP (2004) Cancer immunotherapy: moving beyond current vaccines. Nat Med 10: 909–915.
26. Huang SK, Okamoto T, Morton DL, Hoon DS (1998) Antibody responses to melanoma/melanocyte autoantigens in melanoma patients. J Invest Dermatol 111: 662–667.
27. Forgber M, Trefzer U, Sterry W, Walden P (2009) Proteome serological determination of tumor-associated antigens in melanoma. PLoS One 4: e5199.
28. Ehlken H, Schadendorf D, Eichmuller S (2004) Humoral immune response against melanoma antigens induced by vaccination with cytokine gene-modified autologous tumor cells. Int J Cancer 108: 307–313.
29. Brown A, Bernier G, Mathieu M, Rossant J, Kothary R (1995) The mouse dystonia musculorum gene is a neural isoform of bullous pemphigoid antigen 1. Nat Genet 10: 301–306.
30. Young KG, Kothary R (2007) Dystonin/Bpag1-A link to what? Cell Motil Cytoskeleton 64: 897–905.
31. Lee CW (2000) An extract of cultured A431 cells contains major tissue antigens of autoimmune bullous diseases. Br J Dermatol 143: 821–823.
32. Schuetz CS, Bonin M, Clare SE, Nieselt K, Sotlar K, et al. (2006) Progression-specific genes identified by expression profiling of matched ductal carcinomas in situ and invasive breast tumors, combining laser capture microdissection and oligonucleotide microarray analysis. Cancer Res 66: 5278–5286.
33. Ram M, Shoenfeld Y (2007) Harnessing Autoimmunity (Vitiligo) to Treat Melanoma: A Myth or Reality? Ann N Y Acad Sci 1110: 410–425.
34. Bystryn JC (1989) Serum antibodies in vitiligo patients. Clin Dermatol 7: 136–145.
35. Oyarbide-Valencia K, van den Boorn JG, Denman CJ, Li M, Carlson JM, et al. (2006) Therapeutic implications of autoimmune vitiligo T cells. Autoimmun Rev 5: 486–492.
36. Gogas H, Ioannovich J, Dafni U, Stavropoulou-Giokas C, Frangia K, et al. (2006) Prognostic significance of autoimmunity during treatment of melanoma with interferon. N Engl J Med 354: 709–718.
37. Kim R, Emi M, Tanabe K (2006) Cancer immunosuppression and autoimmune disease: beyond immunosuppressive networks for tumour immunity. Immunology 119: 254–264.
38. Ko K, Yamazaki S, Nakamura K, Nishioka T, Hirota K, et al. (2005) Treatment of advanced tumors with agonistic anti-GITR mAb and its effects on tumor-infiltrating Foxp3+CD25+CD4+ regulatory T cells. J Exp Med 202: 885–891.
39. Wei WZ, Jacob JB, Zielinski JF, Flynn JC, Shim KD, et al. (2005) Concurrent induction of antitumor immunity and autoimmune thyroiditis in CD4+ CD25+ regulatory T cell-depleted mice. Cancer Res 65: 8471–8478.

Table 1
Amounts of hair follicles at different cycle phases observed on histological sections of skin in mice of different genotypes. The day when the morphology of more than 50% of reviewed hair follicles first corresponded to the criteria of a given phase was considered the first day of this phase. *Note*: $N = 40$.

Age (days)	Anagen (%)	Catagen (%)	Telogen (%)
+/+ +/+ +/+ (C57BL/6)			
7	100	0	0
16	5	95	0
20	0	27	73
28	66	0	34
40	24	72	3
+/+ *we/we wal/wal*			
9	77	23	0
12	0	100	0
20	0	26	74
24	84	0	4
32	38	62	0
60	13	32	55
$Fgf5^{go\text{-}Y}/Fgf5^{go\text{-}Y}$ *we/we wal/wal*			
16	100	0	0
18	38	62	0
24	5	72	23
26	66	13	21
32	38	62	0
38	3	18	79

end of anagen phase (Fig. 1A). However, in contrast to *Bmp2* expression level, the level of *Id1* expression in first hair cycle begins increasing just at telogen phase. The second increase in *Id1* expression accounts for next anagen phase (35 days after birth). *Id1* gene is the target gene for BMP signaling pathway, and the activity of this pathway may be assessed on the basis of its expression [6].

In *we/we wal/wal* mutant mice, durations of anagen (12 days) and telogen (4 days) are decreased, but catagen (8 days), conversely, is longer than in normal mice (Table 1). Peaks of *Bmp2* and *Id1* expression in skin of *we/we wal/wal* are observed at catagen phase but not at telogen, as they are in C57BL/6 mice (Fig. 1B). During short anagen phases of G1 and G2 guard hair in *we/we wal/wal* mice, levels of *Bmp2* and *Id1* genes mRNA decrease. In normal mice, conversely, local peaks of expression of these genes are observed at these phases. The data about expression of *Bmp2* and *Id1* genes correspond to the results of histological assay and to the phenotype of *we/we wal/wal* mice. Elevation of expression of *Bmp2* and *Id1* gene in mice older than 14 days is conducted by intense hair loss at early catagen phase. After shedding of first generation hair in *we/we wal/wal* mice, physiological cycle of hair follicles terminates, and at that point the expression of BMP-dependent target gene, *Id1*, can be hardly detected. It has been also found that in skin of *we/we wal/wal* mice, levels of mRNA of *Bmp2* and *Id1* genes were approximately three times higher than in norm. Thus, hair loss and the disorder of hair cycle in *we/we wal/wal* mice might be conducted by disruption of cyclic changes in BMP signaling pathway and its over-activation.

$Fgf5^{go\text{-}Y}$ gene, while interacting with *we* and *wal* genes in triple homozygotes, results in prolongation of anagen (18 days) and catagen (6 days) of G1 guard hair, as compared to the duration of these phases in *we/we wal/wal* mice (**Table 1**). *Bmp2* gene expression dynamics in skin of $Fgf5^{go\text{-}Y}/Fgf5^{go\text{-}Y}$ *we/we wal/wal* mice generally corresponds to such in skin of *we/we wal/wal* mice, but additional peak of *Bmp2* mRNA level is observed in triple homozygous mice at the age of 45 days (Fig. 1C). At the same time, the expression of *Id1* gene reaches its maximum just in late catagen in triple mutants. This suggests that mutant $Fgf5^{go\text{-}Y}$ gene might have the influence on downstream members of BMP pathway. Mutant $Fgf5^{go\text{-}Y}$ gene causes reduction of *Id1* gene expression, thereby weakening the effects of interaction between *we* and *wal* mutant genes and resulting in partial recovery of hair growth.

In conclusion, our results show that genes *Fgf5*, *we*, and *wal* are required for normal cyclic expression of BMP-associated genes *Bmp2* and *Id1* in skin, according to current phase of hair cycle in mice.

References

[1] Müller-Röver S, Handjiski B, Carina van der Veen, Eichmuller S, Foitzik K, McKay I, et al. A comprehensive guide for the accurate classication of murine hair follicles in distinct hair cycle stages. J Invest Dermatol 2001;117:3–15.
[2] Konyukhov BV, Malinina NA, Martynov MIu. The *we* gene is a modifier of the *wal* gene in mice. Genetika 2004;40(7):68–74.
[3] Konyukhov BV, Nesterova AP, Malinina NA. The angora gene weakens the effect of interaction of the mutant genes wellhaarig and waved alopecia in mice. Genetika 2009;45(5):717–20.
[4] Yuhki M. BMPR1A signaling is necessary for hair follicle cycling and hair shaft differentiation in mice. Development 2004;131:1825–33.
[5] Freeman TC, Dixon AK, Campbell EA, Tait TM, Richardson PJ, Rice KM, et al. Expression Mapping of Mouse Genes. MGI Direct Data Submission 1998.
[6] Plikus MV, Mayer JA, de la Cruz D, Baker RE, Maini PK, Maxson R, et al. Cyclic dermal BMP signalling regulates stem cell activation during hair regeneration. Nature 2008;451:340–5.

Anastasia Nesterova*
Igor Nizamutdinov
Pavel Golovatenko-Abramov
Boris Konyukhov
Laboratory of Developmental Genetics, Vavilov Institute of General Genetics, Russian Academy of Sciences, Moscow, Russian Federation

*Corresponding author. Tel.: +7 499 135 4192; fax: +7 499 132 8962

E-mail address: nesterova.anastasia@gmail.com (A. Nesterova)

26 April 2010

doi:10.1016/j.jdermsci.2010.10.002

Letter to the Editor

Relation between the expression levels of the POU transcription factors Skn-1a and Skn-1n and keratinocyte differentiation

Keratinocyte proliferation and differentiation are tightly regulated by cellular transcription factors, including activator protein (AP)-1 family proteins [1], nuclear factor-kappa B family proteins [2], cytidine–cytidine–adenosine–adenosine–thymidine (CCAAT)/enhancer binding proteins (C/EBPs) [3], p53-related proteins [4], and POU transcription factors [5]. Three POU transcription factors—Oct-1, Oct-6, and Skn-1a—are expressed in the epidermis. Among them, the Skn-1a gene is primarily expressed in the epidermis and is thought to play a critical role in keratinocyte differentiation and proliferation [6].

We have recently identified Skn-1n, a novel splice variant of Skn-1a. Sequence analysis revealed that Skn-1n mRNA contained an additional 112-bp sequence in the 5′ region as compared to

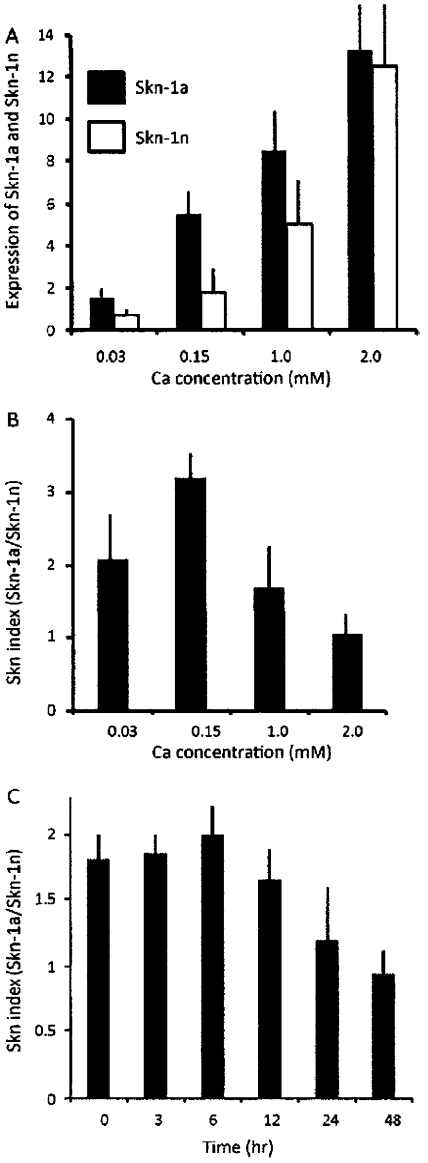

Fig. 1. Skn-1a and Skn-1n mRNA expression. Normal human epidermal keratinocytes were cultured in a standard serum-free keratinocyte growth medium containing 0.03 mM calcium. The subconfluent cultured cells were incubated for 48 h in media containing 0.03 mM, 0.15 mM, 1.0 mM, or 2.0 mM calcium (A and B). Before harvesting, cultures were incubated for 1, 3, 6, 12, 24, or 48 h in media containing 2.0 mM calcium (C). Total RNA was extracted from keratinocytes using the RNeasy kit (Qiagen, Hilden, Germany), and cDNA was reverse transcribed from 0.5 μg total RNA. Real-time RT-PCR analysis of Skn-1a, Skn-1n, and glyceraldehyde-3-phosphate dehydrogenase expression was performed using primers described previously [7]. Continuous quantitative measurement of the PCR products was achieved by using SYBR Green fluorescent dye (Opticon 2, Bio-Rad, Hercules, CA). The expression level of each gene was normalized to the corresponding glyceraldehyde-3-phosphate dehydrogenase level. The results are expressed as mean (SD). Representative data for 3 independent experiments are shown here.

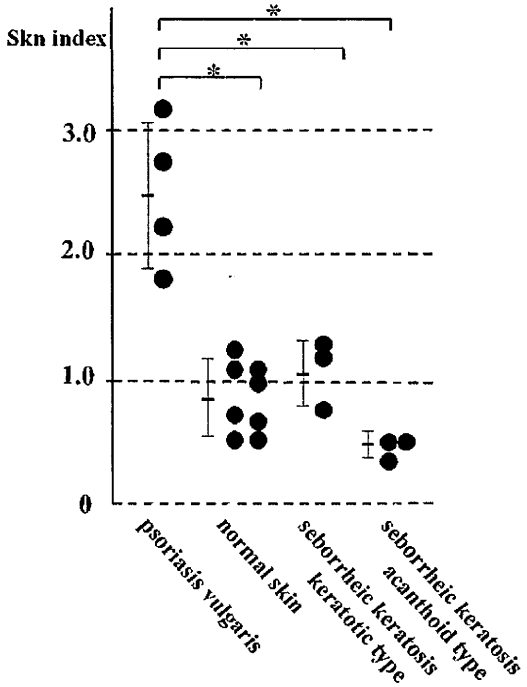

Fig. 2. Skn index in normal skin and psoriasis vulgaris and seborrheic keratosis skin lesions. Skin biopsy specimens of the affected regions were obtained from patients with psoriasis vulgaris and seborrheic keratosis (keratotic and acanthotoid types). Normal skin specimens were also taken from normal individuals. Dispase treatment was used to separate the epidermis from the dermis in the normal skin and psoriatic lesion samples. In samples from patients with seborrheic keratosis, we used a scalpel to remove the dermis underlying the lesions. After RNA extraction, we performed real time RT-PCR (as mentioned above). The Skn index is represented as mean (SD). Statistical analysis of differences was performed using unpaired Student's *t*-test. The Skn indices of the psoriasis vulgaris samples were significantly higher than those of the normal skin and seborrheic keratosis samples ($^*p < 0.01$). No statistically significant difference was observed in the Skn indices between patients with the keratotic and acanthoid types of seborrheic keratosis.

Skn-1a mRNA. A novel initiation codon in sequence was found in this 112-bp sequence [7]. Although these sequence data suggested a functional difference between Skn-1a and Skn-1n, the significance and function of Skn-1n has not yet been elucidated even in terms of keratinocyte differentiation. Skn-1a transactivates the promoters for the K10 and SPRP2A genes that are expressed during keratinocyte differentiation, and therefore Skn-1a may accelerate keratinocyte differentiation [6]. Previously, we reported that the mRNA expression of both Skn-1a and Skn-1n increased in cultured normal human keratinocytes after calcium-induced differentiation, suggesting that the function of Skn-1n might be similar to that of Skn-1a [7]. In this study, we have attempted to clarify the regulation of Skn-1a and Skn-1n expression in order to further understand the roles of these transcription factors in keratinocyte differentiation.

First, we performed reverse transcription (RT)-polymerase chain reaction (PCR) using human keratinocytes cultured at varying calcium concentrations. As shown in our previous study, mRNA expression of both Skn-1a and Skn-1n was upregulated with an increase in calcium concentrations [7]. We also tried to examined isoforms of Skn-d, but failed to detect the bands in our system. In this study, we defined the ratio of the expression of Skn-1a and Skn-1n (Skn-1a/Skn-1n) as the Skn index, which was estimated for each calcium concentration. Normal human keratinocytes were cultured in a keratinocyte growth medium containing 0.03 mM calcium; subconfluent cultured cells were then incubated for 48 h in media containing 0.03, 0.15, 1.0, or 2.0 mM calcium (Fig. 1A and B). The expression level of Skn-1a was twice that of Skn-1n when the cells were cultured in 0.03 mM calcium, whereas both levels were almost identical in cells cultured in 2.0 mM calcium. The Skn index at 0.15 mM calcium was greater than 3.0. Next, RT-PCR was performed using keratinocytes that had been cultured in a keratinocyte growth

medium containing an initial concentration of 0.03 mM calcium, which was later increased to 2.0 mM. The Skn index started decreasing 24 h after the change in calcium concentration and was approximately 50% of the index calculated for the untreated samples after 48 h of incubation (Fig. 1C).

Next, we analyzed in vivo Skn-1a and Skn-1n mRNA expression by using specimens of the normal skin and specimens obtained from patients with seborrheic keratosis (benign skin lesions with varying degrees of keratinization) and psoriasis vulgaris (multifactorial hyperproliferative inflammatory skin disorder). To confirm the predominant expression of Skn-1a and Skn-1n in the epidermis, we treated the normal skin and psoriatic lesion skin samples with dispase to separate the epidermis from the dermis. However, for the seborrheic keratosis samples, we used a scalpel to remove the dermis underlying the lesions. The Skn indices of normal skin samples ranged from 0.48 to 1.16. Moreover, the Skn indices of samples from the psoriatic lesions (range, 1.82–3.08) were significantly higher than those of all the other samples. Among patients with seborrheic keratosis, the Skn indices of those with the keratotic type (range, 0.81–1.29) had no significant difference from the indices of those with the acanthothoid type (range, 0.52–0.62) (Fig. 2).

Skn-1a, an epidermal POU transcription factor, plays a critical role in differentiation-specific gene regulation in epidermal keratinocytes. It is possible that Skn-1a and the related isoforms have different functions in keratinocyte differentiation and proliferation. Previous report showed full-length Skn-1a significantly inhibited K14 promoter activity [8]. However, the deletion of N-terminus leaded to reducing promoter activity to a lesser extent whereas the deletion of C-terminus did not alter suppression activity of the promoter [8]. In this study the RT-PCR experiment showed that expression of Skn-1a was higher than that of Skn-1n in lower calcium concentrations. Expression of Skn-1a was 3 times as much as that of Skn-1n at 0.15 mM calcium concentration, which is the critical point where keratinocytes initiate differentiation in *in vitro* calcium shift experiment. This result suggested that Skn-1a might keep keratinocytes from differentiation rather than Skn-1n. Additional functional analysis of Skn-1a and Skn-1n will be needed for further understanding these transcription factors.

Interestingly, the Skn indices of the psoriasis vulgaris samples were significantly higher than those of normal skin. The epidermis in the patients with psoriasis includes compartments of undifferentiated and proliferating keratinocytes. These suggested that Skn-1a was associated with undifferentiated proliferating keratinocytes to a greater extent than Skn-1n. Those *in vivo* data were compatible with the data from the above mentioned *in vitro* studies performed using cultured keratinocytes. In the case of seborrheic keratosis, however, the Skn indices of the samples from both the keratotic and acanthothoid types were within the range of the Skn indices of normal skin. Although keratotic types of seborrheic keratosis are covered with hard keratinous materials, differentiation degree of total cells in keratotic types is almost similar to those in acanthoid type and normal skin.

We have recently shown some information that keratinocyte proliferation and differentiation are tightly associated with the expression of various differentiation-specific genes [9,10]. In this study, we used the Skn index to determine the difference between normal skin and that affected skin diseases. This index may be a useful tool for evaluating keratinocyte proliferation and differentiation under physiological and pathological conditions. Further investigation of the functions of these epidermal POU transcription factors should provide novel insights into epidermal biology as well as a better understanding of skin diseases.

Conflicts of interest

None declared.

Acknowledgments

The authors thank Yoko Chiba and Yuka Toyomaki for their assistance. This study was supported by grants from the Japanese Ministry of Education, Science and Culture and the Ministry of Public Welfare, Japan.

References

[1] Eckert RL, Crish JF, Robinson NA. The epidermal keratinocyte as a model for the study of gene regulation and cell differentiation. Physiol Rev 1997;77:397–424.
[2] Ryan AK, Rosenfeld MG. POU domain family values: flexibility, partnerships, and developmental codes. Genes Dev 1997;11:1207–25.
[3] Seitz CS, Lin Q, Deng H, Khavari PA. Alterations in NF-kappaB function in transgenic epithelial tissue demonstrate a growth inhibitory role for NF-kappaB. Proc Natl Acad Sci USA 1998;95:2307–12.
[4] Okuyama R, Tagami H, Aiba S. Notch signaling: its role in epidermal homeostasis and in the pathogenesis of skin diseases. J Dermatol Sci 2008;49:187–94.
[5] Maytin EV, Lin JC, Krishnamurthy R, Batchvarova N, Ron D, Mitchell PJ, et al. Keratin 10 gene expression during differentiation of mouse epidermis requires transcription factors C/EBP and AP-2. Dev Biol 1999;216:164–81.
[6] Andersen B, Schonemann MD, Flynn SE, Pearse 2nd RV, Singh H, Rosenfeld MG. Skn-1a and Skn-1i: two functionally distinct Oct-2-related factors expressed in epidermis. Science 1993;260:78–82.
[7] Nakajima K, Tamai K, Yamazaki T, Toyomaki Y, Nakano H, Uitto J, et al. Identification of Skn-1n, a splice variant induced by high calcium concentration and specifically expressed in normal human keratinocytes. J Invest Dermatol 2008;128:1336–9.
[8] Sugihara TM, Kudryavtseva EI, Kumar V, Horridge JJ, Andersen B. The POU domain factor Skn-1a represses the keratin 14 promoter independent of DNA binding. J Biol Chem 2001;276:33036–44.
[9] Aizu T, Tamai K, Nakano H, Rokunohe D, Toyomaki Y, Uitto J, et al. Calcineurin/NFAT-dependent regulation of 230-kDa bullous pemphigoid antigen (BPAG1) gene expression in normal human epidermal keratinocytes. J Dermatol Sci 2008;51:45–51.
[10] Yamamoto C, Tamai K, Nakano H, Matsuzaki Y, Kaneko T, Sawamura D. Vitamin D3 inhibits expression of bullous pemphigoid antigen 1 through post-transcriptional mechanism without new protein synthesis. J Dermatol Sci 2008;50:155–1558.

Hironobu Takemoto
Katsuto Tamai
Eijiro Akasaka
Daiki Rokunohe
Noriko Takiyoshi
Noriko Umegaki
Koji Nakajima
Takayuki Aizu
Takahide Kaneko
Hajime Nakano
Daisuke Sawamura*
Department of Dermatology,
Hirosaki University School of Medicine,
5 Zaifu-cho,
Hirosaki, Aomori 036-8562, Japan

*Corresponding author. Tel.: +81 172 39 5087;
fax: +81 172 37 6060
E-mail address: smartdai@cc.hirosaki-u.ac.jp
derma@cc.hirosaki-u.ac.jp
(D. Sawamura)

9 June 2010

doi:10.1016/j.jdermsci.2010.10.006

JAPANESE DERMATOLOGICAL ASSOCIATION
THE JOURNAL OF DERMATOLOGY

doi: 10.1111/j.1346-8138.2010.01008.x

Journal of Dermatology 2011; **38**: 489–492

CASE REPORT

Exon 87 skipping of the *COL7A1* gene in dominant dystrophic epidermolysis bullosa

Hiroshi KOGA,[1] Takahiro HAMADA,[1] Norito ISHII,[1] Shunpei FUKUDA,[1] Sachiko SAKAGUCHI,[1] Hajime NAKANO,[2] Katuto TAMAI,[3] Daisuke SAWAMURA,[2] Takashi HASHIMOTO[1]

[1]*Department of Dermatology, Kurume University School of Medicine, Asahimachi, Kurume, Fukuoka,* [2]*Department of Dermatology, Hirosaki University Graduate School of Medicine, Hirosaki, and* [3]*Division of Gene Therapy Science, Department of Molecular Therapeutics, Osaka University Graduate School of Medicine, Osaka, Japan*

ABSTRACT

Dystrophic epidermolysis bullosa (DEB) is a rare, inherited, blistering disorder resulting from mutations in the *COL7A1* gene, which encodes the anchoring fibrils, type VII collagen. We herein describe a further Japanese girl diagnosed with dominant DEB (DDEB). She had blisters sporadically and erosions healed with mild scarring and milia on the knees and pretibial regions. Severe pruritus was present at this time. Direct nucleotide sequencing of genomic DNA disclosed a heterozygous same splice-site mutation c.6900G>A in the *COL7A1*, which causes in-frame exon 87 skipping. So far, five different *COL7A1* mutations leading to exon 87 skipping have been identified in rare forms of DEB: four DDEB pruriginosa and one pretibial DDEB. Therefore, a recent study suggested that exon 87 skipping in *COL7A1* was related to the phenotype of DDEB pruriginosa. When she was 18 years old, however, the blister formation and pruritus markedly decreased. Therefore, her clinical symptoms were consistent to very mild DDEB but not to DDEB pruriginosa. Taken together, in-frame exon 87 skipping through c.6900G>A mutation may account for the mild skin features, rather than DDEB pruriginosa, in the present case.

Key words: *COL7A1*, dystrophic epidermolysis bullosa, genodermatosis, genotype–phenotype correlation, pruriginosa.

INTRODUCTION

Dystrophic epidermolysis bullosa (DEB) is a rare inherited blistering disorder resulting from mutations in the *COL7A1* gene, which encodes type VII collagen, the major component of anchoring fibrils at the dermal–epidermal junction. Over 300 pathogenic mutations have been described within *COL7A1* in various clinical forms of DEB. So far, five different *COL7A1* mutations leading to exon 87 skipping have been identified in rare forms of DEB: four dominant DEB (DDEB) pruriginosa and one pretibial DDEB.[1–4] Therefore, a recent study suggested that exon 87 skipping in *COL7A1* was related to the phenotype of DDEB pruriginosa.[5] We herein describe a further DDEB patient with the same splice-site mutation c.6900G>A, but the clinical appearance of the patient was quite different from that of DDEB pruriginosa.

CASE REPORT

The patient was a Japanese girl who was the offspring of healthy unrelated parents. She presented with a history of trauma-induced skin blistering and erosions mainly on the extremities at the age of

Correspondence: Takashi Hashimoto, M.D., Department of Dermatology, Kurume University School of Medicine, 67 Asahimachi, Kurume, Fukuoka 830-0011, Japan. Email: hashimot@med.kurume-u.ac.jp
Received 23 February 2010; accepted 11 May 2010.

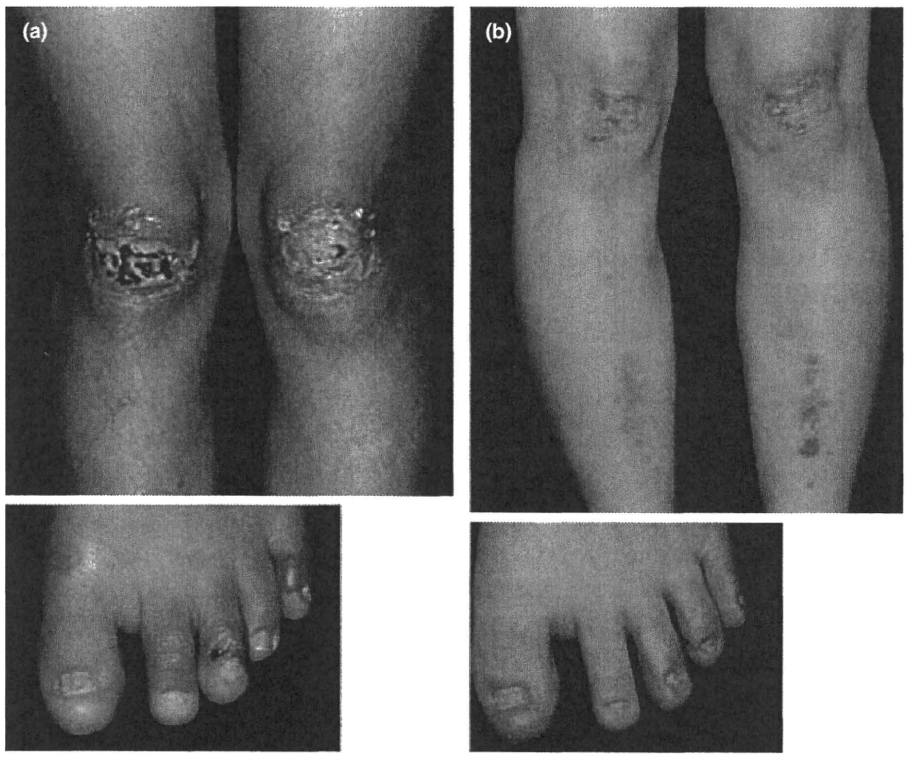

Figure 1. Clinical features of the patient. (a) Erosions healed with mild scarring on the knee, and blisters and nail dystrophy were seen on the toes at 8 years of age. (b) Symptoms were markedly improved by 18 years of age.

1 month. She also had nail dystrophy. She was referred to our hospital when she was 8 years old. There were scattered blistering and erosions healed with mild scarring and milia on the knees and pretibial regions (Fig. 1a). Severe pruritus was initially present. However, blister formation and pruritus markedly decreased by 18 years of age (Fig. 1b). The clinical manifestations of this patient were consistent to very mild DDEB but not to DDEB pruriginosa. Direct nucleotide sequencing of genomic DNA from the patient disclosed a heterozygous G to A transition at nucleotide c.6900 that does not lead to an amino acid change in p.Gln2300 residue (Fig. 2a). Reverse transcription polymerase chain reaction (RT–PCR) across the site of the c.6900G>A transition identified two bands of 475 and 544 bp in size, compared to a single 544 bp band in the normal control (Fig. 2b). Subcloning and direct sequencing disclosed that the 475-bp band was a mutant transcript with in-frame exon 87 skipping (Fig. 2c). In contrast to the previous report by Saito *et al.*,[5] we further detected two additional aberrant transcripts with inclusion of the entire intron 86 or 87 as a new exon, leading to premature termination codon 27 or 120 bp downstream, respectively (Fig. 2c). The 544-bp band was the normal wild-type transcript.

DISCUSSION

As Saito *et al.* described,[5] it seems to be probable that exon 87 skipping is related to the phenotype of DDEB pruriginosa. However, the present case was clinically quite different from DDEB pruriginosa, although she was shown to have exon 87 skipping by RT–PCR analysis. Inter- and intrafamilial variability from the same *COL7A1* mutations has been previously described in the published work. For example, the most common *COL7A1* mutation p.Gly2043Arg has been identified in a different phenotype of DDEB.[6] It is plausible that modifying genes, epigenetic or environmental factors might influence the phenotypic variations in DEB. Therefore, genetic counseling in such cases is fraught with difficulty. It is important that families are made aware of the

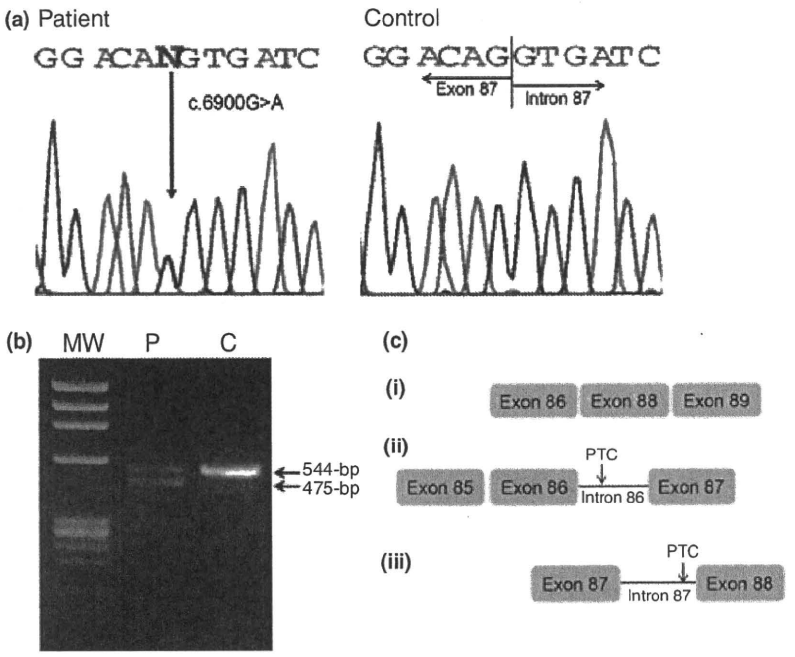

Figure 2. Molecular basis of dominant dystrophic epidermolysis bullosa (DEB) in the present patient (a) Direct nucleotide sequencing of genomic DNA from the patient disclosed a heterozygous G>A transition at nucleotide c.6900. (b) Reverse transcription polymerase chain reaction (RT–PCR) across the site of the c.6900G>A transition. In the amplified cDNA from control (lane C), a single band of 544 bp was present. By contrast, in the amplified cDNA from the patient (lane P), two different bands of 544 and 475 bp were identified. (c) Subcloning and direct sequencing revealed the band of 475 bp is a mutant transcript with in-frame exon 87 skipping. Two aberrant mutant transcripts with inclusion of the entire intron 86 or 87 were also identified, although the bands were not visible on the agarose gel, shown in (b). PTC, premature termination codon.

clinical diversity in DEB and are offered appropriate counseling.

The RT–PCR analysis in this study revealed two aberrant mutant transcripts with inclusion of the entire intron 86 or 87 as a new exon, as well as exon 87 skipping. However, the RT–PCR bands of these two mutant transcripts were not visible on the agarose gel, suggesting low mRNA expression of these mutants in the patient's skin. Taken together, in-frame exon 87 skipping through c.6900G>A mutation may account for the mild skin features, rather than DDEB pruriginosa, in the present case.

ACKNOWLEDGMENTS

We are grateful to Miss Ayumi Suzuki and Miss Takako Ishikawa for technical assistance, and Miss Akiko Tanaka and Mrs Yasuko Nakayama for secretarial work. We thank the patients for their participation. This work was supported by Grants-in-Aid for Scientific Research and Strategic Research Basis Formation Supporting Project from the Ministry of Education, Culture, Sports, Science and Technology of Japan, by Health and Labor Sciences Research Grants and grants for Research on Intractable Diseases from the Ministry of Health, Labor and Welfare of Japan. This work was also supported by grants from the Uehara Memorial Foundation, the Nakatomi Foundation, the Kaibara Medical Foundation, the Japan Lydia O'leary Memorial Foundation, and the Japanese Dermatological Association (Shiseido Award).

REFERENCES

1 Sakuntabhai A, Hammanmi-Hausli N, Bodemer C *et al.* Deletion within *COL7A1* exons distant from consensus splice sites alter splicing and produce shortened polypeptides in dominant dystrophic epidermolysis bullosa. *Am J Hum Genet* 1998; **63**: 737–748.

2 Mellerio JE, Ashton GHS, Mohammedi R *et al.* Allelic heterogeneity of dominant and recessive *COL7A1* mutations

underlying epidermolysis bullosa pruriginosa. *J Invest Dermatol* 1999; **112**: 984–987.
3 Jiang W, Bu D, Yang Y *et al.* A novel splice site mutation in collagen type VII gene in a Chinese family with dominant dystrophic epidermolysis bullosa pruriginosa. *Acta Derm Venereol* 2002; **82**: 187–191.
4 Drera B, Castiglia D, Zoppi N *et al.* Dystrophic epidermolysis bullosa pruriginosa in Italy: clinical and molecular characterization. *Clin Genet* 2006; **70**: 339–347.
5 Saito M, Masunaga T, Ishiko A. A novel *de novo* splice-site mutation in the *COL7A1* gene in dominant dystrophic epidermolysis bullosa (DDEB): specific exon skipping could be a prognostic factor for DDEB prurigonosa. *Clin Exp Dermatol* 1999; **34**: e934–e936.
6 Mellerio JE, Salas-Alanis JC, Talamantes ML *et al.* A recurrent glycine substitution mutation, G2043R, in the type VII collagen gene (*COL7A1*) in dominant dystrophic epidermolysis bullosa. *Br J Dermatol* 1998; **139**: 730–737.

Arch Virol
DOI 10.1007/s00705-011-0938-7

ORIGINAL ARTICLE

Methyl-beta cyclodextrin alters the production and infectivity of Sendai virus

Hiroshi Fujita · Katsuto Tamai · Masako Kawachi · Kotaro Saga · Takashi Shimbo · Takehiko Yamazaki · Yasufumi Kaneda

Received: 5 August 2010 / Accepted: 22 January 2011

Abstract Cellular membrane cholesterol has been shown to support various membrane proteins. However, the role and function of membrane cholesterol in viral production are still unclear. Here, we investigated the effects of cholesterol depletion from the cell membrane on the production of hemagglutinating virus of Japan (HVJ; Sendai virus). Cholesterol depletion from LLC-MK2 cells by methyl-beta cyclodextrin treatment resulted in a marked increase in the production of both HVJ from the infected cells and virus-like particles from M-gene-transfected cells. The HVJ produced from cholesterol-depleted cells possessed a reduced amount of envelope cholesterol and showed a rather wide range of particle sizes and amount of envelope protein compared to HVJ produced from untreated cells. Direct depletion of envelope cholesterol from HVJ significantly impaired its infectivity, even without a change in envelope protein composition. These results suggest that membrane cholesterol plays important roles in regulating the production of infectious HVJ.

Introduction

Cholesterol-rich microdomains on the cell membrane, called lipid rafts, have been shown to function in regulating the production of various viruses [4]. However, cholesterol depletion from infected cells affects the production of each virus differently. A recent study reported that cholesterol depletion from the cell membrane promotes the budding of influenza virus [3]. Because the hemagglutinin and neuraminidase glycoproteins of influenza virus have an intrinsic affinity for lipid rafts, cholesterol depletion has been suggested to release raft-trapped hemagglutinin and neuraminidase to be dispersed on the cell surface and to accelerate budding of virions [20, 32, 38]. Measles virus has also been shown to bud in places other than cholesterol-rich regions of cells [22]. However, in the case of Semliki Forest virus, membrane cholesterol depletion has been shown to dramatically reduce viral production [21]. Production of human immunodeficiency virus-1 is also significantly reduced by cholesterol depletion in cells expressing Gag protein [23, 27, 28].

Hemagglutinating virus of Japan (HVJ), also called Sendai virus, belongs to the genus *Respirovirus* of the family *Paramyxoviridae*. The genome of HVJ is a linear and non-segmented negative-strand RNA of approximately 15.4 kb, containing six major genes that are arranged in tandem. This genome is tightly encapsulated with nucleoprotein and is further complexed to phosphoprotein and large protein (L protein). This ribonucleoprotein complex constitutes the internal core structure of the virion. The viral envelope contains two spike proteins: hemagglutinin-neuraminidase (HN) protein, which mediates the attachment of virions, and fusion (F) protein, which mediates the penetration of ribonucleoproteins into the infected cells. The M protein functions in virus assembly and budding [6].

HVJ infects and replicates independently of cellular nuclear functions and without reverse transcription during its life cycle in most mammalian cells, which is beneficial for analysis of factors related to virus production, such as membrane cholesterol [17]. A previous study demonstrated that cholesterol depletion from the cell membrane increases the proportion of M protein in the HVJ protein

H. Fujita · K. Tamai · M. Kawachi · K. Saga · T. Shimbo · T. Yamazaki · Y. Kaneda (✉)
Division of Gene Therapy Science, Graduate School of Medicine, Osaka University, 2-2 Yamadaoka, Suita, Osaka 565-0871, Japan
e-mail: kaneday@gts.med.osaka-u.ac.jp

Published online: 11 February 2011

population [7]. Because M protein is believed to function in the budding phase HVJ virion assembly [1], this cholesterol-depletion-dependent increase in M protein in HVJ may affect HVJ production. However, no data have yet been provided concerning the relationship between cell membrane cholesterol and HVJ production.

In the present study, we investigated the effects of cholesterol depletion from the host cell membrane on HVJ production, using methyl-beta cyclodextrin (MβCD). We found evidence that membrane cholesterol plays critical roles in infectious HVJ production.

Materials and methods

Cell culture

The Rhesus monkey kidney cell line LLC-MK2 was cultured in modified Eagle's medium (Gibco-BRL, Rockville, MD, USA) containing 10% fetal bovine serum, 100 units/ml penicillin, and 0.1 mg/ml streptomycin. The cell line was cultured in a humidified atmosphere of 5% CO_2/95% air at 37°C.

Antibodies

The monoclonal antibody directed against the F protein [35] was kindly provided by H. Taira (Department of Bioscience and Technology, Faculty of Agriculture, Iwate University, Morioka, Japan). Rabbit polyclonal antibodies against HN and M proteins were generated by Hokkaido System Science Co. Ltd. (Sapporo, Japan), using peptide antigens of HN and M proteins. The peptide sequence of HN was 276-VDERTDYSSDGIED-289, and that of the M protein was 23-LRTGPDKKAIPHIRC-36.

Viruses

HVJ (VR-105 parainfluenza1 Sendai/52, Z strain) was purchased from American Type Culture Collection (Manassas, VA, USA), amplified in the choriallantoic fluid of 10- to 14-day-old chick eggs, and purified by centrifugation as described previously [12]. Harvested HVJ was estimated using the hemagglutinating activity (HA) assay. Serial two-fold dilutions of a 50-μl HVJ suspension from untreated LLC-MK2 cells or cells treated with MβCD were mixed in 96-well U-bottom plates. A 1% suspension of chicken red blood cells (50 μl) was added to each well, followed by incubation for 1 h at 4°C. Hemagglutination in each well was then observed, and the hemagglutinating titer (hemagglutinating assay units [HAU]/ml) was calculated [36].

Trypan blue staining

Cell viability was determined by trypan blue staining. Cells were washed with phosphate-buffered saline (PBS) and mixed with an equal volume of PBS and 0.5% trypan blue (Nacalai Tesque Inc., Kyoto, Japan) for 2 min and then examined by light microscopy [37].

Infection of cells

Virus was harvested from 15-cm-diameter plates. A total of 8×10^6 LLC-MK2 cells were plated 24 h before HVJ infection. LLC-MK2 cells were infected with wild-type HVJ for 1 h at 37°C. The cells were washed with PBS and then incubated for 20 h at 37°C with 10% FBS MEM, after which serum-free modified Eagle's medium containing 1% (7.67 mM) MβCD (Sigma Aldrich, Tokyo, Japan), penicillin (100 units/ml), and streptomycin (0.1 mg/ml) was added. For the HA-HR-B (heptad repeat-B) peptide [30] experiments, HA-HR-B peptides at a final concentration of 140 nM were added to LLC-MK2 cells at an m.o.i. of 10. Six hours after treatment with serum-free MEM containing 1% MβCD at 37°C, extracellular virus was harvested. Viral supernatant was briefly clarified at 440 × g for 5 min and then passed through a 1.2-μm-pore-size filter. The filtered supernatant was centrifuged at 20,400 × g for 30 min, and the pellet was then resuspended in PBS.

Detection of vesicles in culture medium

We used 60 μl of Transfectin reagent (Bio-rad, Hercules, CA, USA) and 12 μg of expression vector encoding the M gene or empty vector to transfect LLC-MK2 cells growing in 10-cm dishes. Cells were cultured at 37°C for 24 h, and the medium was then replaced with serum-free Opti-MEM (Gibco-BRL). After 12 h at 37°C, the cells were dissolved in sample buffer (125 mM Tris-HCl [pH 6.8], 10% 2-mercaptoethanol, 4% sodium dodecylsulfate, 10% sucrose, 0.004% bromophenol blue). The culture medium was briefly clarified, and vesicles released into the medium were then purified by ultracentrifugation at 190,000 g for 2 h at 4°C through 4 ml of 30% glycerol in PBS. Vesicles were resuspended in PBS [34].

SDS-PAGE analysis and western blotting

Protein samples were analyzed by SDS-PAGE. After electrophoresis, the proteins were transferred using a semidry system onto Hybond P (GE Healthcare, Little Chalfont Buckinghamshire, UK). Blots were then incubated with specific antibodies, followed by the appropriate horseradish peroxidase (HRP)-coupled secondary antibodies. Protein

detection was performed using the enhanced chemiluminescence system (GE Healthcare).

Immunoelectron microscopy

Virus was suspended in saline, dropped onto a microgrid, dried at room temperature, and fixed sequentially with 1% glutaraldehyde for 30 min and 1% osmium tetroxide for 30 min. Then the grids were washed in PBS and reacted with anti-F antibody as described above. After 1 h, the grids were washed three times with PBS and reacted with goat anti-mouse IgG-gold colloidal particles (10 nm; 1:100; E & Y Laboratory, San Mateo, CA, USA) for 1 h at room temperature. The treated grids were washed with PBS, dried, and stained with 4% uranium acetate for 2 min at room temperature [13, 19].

Northern blot analysis

HVJ genomic RNA was isolated using PURESCRIPT DNA and RNA isolation kits (Gentra Systems, Minneapolis, MN, USA). Total RNA was isolated from LLC-MK2 cells using an RNeasy kit (QIAGEN, Hilden, Germany). Each RNA sample was separated on a formaldehyde/1.2% agarose gel, transferred to Hybond XL membranes (GE Healthcare), and then hybridized with a ^{32}P-labeled antisense cDNA probe to detect transcripts of HVJ mRNA.

Immunofluorescence by confocal microscopy

The HVJ-infected cells were fixed in 4% paraformaldehyde at 4°C for 15 min and permeabilized with 0.1% Triton X-100 at room temperature for 3 min. Cells were then incubated with specific antibodies for 1 h at room temperature, followed by the appropriate horseradish Alexa Fluor 555-coupled secondary antibodies. Then cells were stained with 1 μg/ml DAPI (Sigma Aldrich) and imaged using a confocal laser microscope (Radiance 2100; Bio-Rad Japan, Tokyo, Japan) equipped with Laser Sharp 2000 software [13, 19]. Stained cells were counted using the ImageJ program (National Institute of Health, Bethesda, MD, USA).

Sucrose gradient centrifugation of virions

Harvested HVJ (described above) was centrifuged through 12 ml of a 15-60% (w/v) linear sucrose gradient at 35,000 × g for 90 min. After fractionation into 12 fractions (1 ml each), 20 μl of each fraction was electrophoresed through a 10% SDS-PAGE gel. We used 100 μl of each fraction for northern blot analysis [9]. For solubilization of HVJ envelope, HVJ virions in Tris buffer were treated with 0.25% NP40 at 15-20°C for 15 min [10].

Cholesterol quantification

Cellular and HVJ cholesterol levels were quantified using a cholesterol quantification kit (Cayman Chemical, Ann Arbor, MI, USA). Samples of HVJ solution (5 μl) were used to quantify the HVJ cholesterol.

Fusion assay

LLC-MK2 cells were seeded at a density of 1000 cells/10-cm dish and cultured for 3 days to form colonies. After washing with PBS, wild HVJ was added to one dish at an m.o.i of 1000, and the same volume of HVJ-CD was added to another dish. The cells were incubated at 37°C for 90 min, washed with PBS, and incubated overnight at 37°C in 10% FBS MEM. The cells were then washed in cold PBS, fixed with ice-cold 80% methanol and stained with Giemsa solution (Wako, Osaka, Japan) for 20 min. Fused cells were viewed with a microscope, and the number of colonies containing fused cells was counted.

Purification of HR-B peptides

Escherichia coli strain TOP10 was used for transformation and cloning experiments and for maintenance of plasmid pENTR/SD/D-topo (Invitrogen, Carlsbad, CA, USA). HA-HR-B (HA epitope tag peptide fused to a HR-B sequence)-*E. coli* strain DH5α was used for transformation of pDEST14 (Invitrogen). HA-HR-B-*E. coli* strain BL21 (DE3) was used for the expression of the cloned *HA-HR-B* gene.

HA-HR-B was constructed by polymerase chain reaction amplification of DNA using the following primers: 5'-CACCATGTACCCATACGATGTTCCAGATTAC GCTAACTTGACAGTCGGTCCTGC-3' and 5'-TCATAC CTCCGAGAGGATTTTCC-3'. The amplified HA-HRB fragments were cloned into pENTR/SD/D-topo vector and used in a recombination reaction with the pDEST14 vector. The BL21 (DE3) strain was transformed with cloned pDEST14 HA-HR-B. Overnight pre-cultures in the absence of IPTG were diluted 1:500 in 500 ml LB containing carbenicillin and incubated at 37°C with shaking until the optical density (A_{600} nm) was 0.5-0.6. IPTG was then added, and the incubation was continued for 3 h. Cultured bacteria were spun down and resuspended with sonication buffer (50 mM Tris-HCl, pH 8.0, 50 mM NaCl, 1 mM EDTA, 1 mM DTT). Sonication was performed 10 times for 10 sec each, on ice, and the cells were then spun down and washed. Inclusion bodies were was treated with 8 M urea solution (8 M urea, 50 mM Tris-HCl, pH 8.0, 1 mM DTT, 1 mM EDTA) for 1 h at room temperature and then ultracentrifuged at 40,000 × g for 30 min at 4°C. The supernatants were dialyzed in 4 M urea/2 M urea solution

and sonication buffer at 4°C. Dialyzed samples were ultracentrifuged at 40,000 × g for 30 min at 4°C and then reacted overnight at 4°C with HA-conjugated gels (Sigma Aldrich). The HA resin was poured into a 10-ml open column, and HA-HR-B peptides were solubilized by treatment with 100 mM glycine-HCl, pH 2.5, and equilibrated with one-tenth volume of 1 M Tris. Purified HA-HR-B peptides were analyzed by Tris-Tricine SDS-PAGE and western blotting of the HA-epitope tag.

Results

Effect of MβCD treatment on LLC-MK2 cells

Membrane-embedded cholesterol can be removed by treatment with MβCD [2, 7, 8, 11, 14–16, 25, 27, 29]. To determine the optimal conditions of cholesterol depletion for evaluating HVJ production, we first investigated cell viability after cholesterol depletion from LLC-MK2 cells. LLC-MK2 cell viability after MβCD treatment for various periods and at various doses of MβCD is shown in Fig. 1a. The maximum dose of MβCD (1% w/v) did not have a significant effect on cell viability within 6 h but started to impair cell survival beyond 6 h. We then measured the membrane cholesterol in LLC-MK2 cells at various time points within 6 h after 1% MβCD treatment. The MβCD treatment depleted cholesterol from the LLC-MK2 cell membranes in a time-dependent manner, and about 90% of the cholesterol was depleted by 6 h of MβCD treatment (Fig. 1b). Dose-dependent cholesterol depletion by a 6-h treatment with MβCD was also confirmed (Fig. 1c). Next, HVJ-infected LLC-MK2 cells in the late phase of virus production (20 h post-infection) were treated with different concentrations of MβCD for various treatment periods, and the amounts of HVJ released into the culture medium were then estimated by a hemagglutinating activity assay. Treatment of HVJ-infected LLC-MK2 cells with 1% MβCD markedly increased HVJ production (Fig. 1d). These results, together with those of the cell viability study, demonstrated that 1% MβCD treatment for 6 h provides the maximum effect on HVJ production without affecting LLC-MK2 cell viability.

Effects of cholesterol depletion on HVJ production

We then investigated the effects of MβCD treatment on HVJ production from LLC-MK2 cells more precisely. Released virions were harvested from the supernatant and purified, and viral RNA was extracted. A significant increase in virus production was observed by northern blot analysis of HVJ from the cholesterol-depleted cells (HVJ-CD) that had been treated with 1% MβCD for 6 h (Fig. 2a). Under these conditions, more than 90% of LLC-MK2 cells survived, and about 90% of the total cholesterol was depleted from the cells (Fig. 1a and b). Quantitative analysis of the blot indicated a 5.6-fold induction of HVJ production under the cholesterol-depletion conditions compared to culture without cholesterol depletion (Fig. 2a, right panel). After performing cholesterol depletion in culture, an equal volume of LLC-MK2 cell culture medium containing either wild-type HVJ or HVJ-CD was then subjected to SDS-PAGE and Coomassie blue staining analysis to evaluate the amount of HVJ proteins produced (Fig. 2b). Quantitative analysis of the protein staining showed about a 2- to 4-fold increase in HVJ proteins in the culture medium containing HVJ-CD compared to the medium containing wild-type HVJ.

To investigate whether cholesterol depletion of the HVJ-infected cells affects the envelope protein level, HVJ-infected LLC-MK2 cells were subjected to western blotting for HN and F proteins before and after cholesterol depletion (Fig. 2c). The amounts of HN and F proteins in the HVJ-infected LLC-MK2 cells were not significantly changed by cholesterol depletion, indicating that the increase in HVJ production by cholesterol depletion was not due to the induction of envelope protein by cholesterol depletion.

To assess the effect of MβCD on virus budding in a more simplified system, we utilized virus-like particle (VLP) production by the expression of the M protein of HVJ in LLC-MK2 cells. The M proteins of HVJ interact with each other on the inner surface of the lipid bilayer of the cell membrane to form a sheet that interacts with viral nucleocapsids and glycoproteins. The M protein of HVJ promotes vesiculation of the M protein-lined membrane and the release of M protein-containing particles, so-called virus-like particles (VLP), into the extracellular medium without the aid of other viral proteins [33, 34]. We investigated VLP production by transfecting LLC-MK2 cells with a plasmid vector expressing the M protein of HVJ, followed by incubation with or without MβCD. Because the amount of budded VLP is reflected by the amount of M protein inside the VLP, the amount of VLP production was evaluated by western blotting for M protein. The increase in VLP production from the M-protein-transfected LLC-MK2 cells that had received subsequent MβCD treatment is shown in Fig. 2d. The production of M protein itself in LLC-MK2 cells was not altered by MβCD treatment (Fig. 2d), indicating a direct effect of cellular membrane cholesterol depletion on the budding of VLP. Quantitative imaging analysis of the western blot revealed about a 3-fold increase in VLP budding after MβCD treatment.

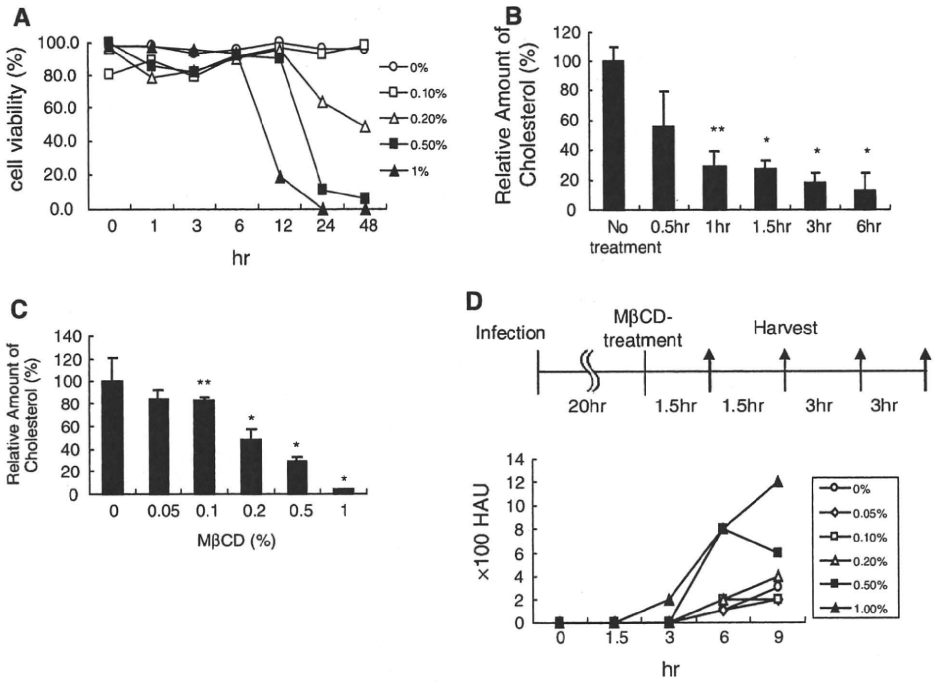

Fig. 1 Effect of MβCD treatment on LLC-MK2 cells. (**a**) LLC-MK2 cell viability was measured at different time points after treatment with serial doses of methyl-beta cyclodextrin (MβCD). (**b**) Quantification of LLC-MK2 cell membrane cholesterol at various time points after 1% MβCD treatment. (**c**) Quantification of LLC-MK2 cell membrane cholesterol after treatment with different amounts of MβCD for 6 h. (**d**) Measurement of hemagglutinating activity in the culture media of HVJ-infected LLC-MK2 cells at various time points after MβCD treatment. HVJ-infected LLC-MK2 cells in the late phase of viral production (20 h post-infection) were treated with different concentrations of MβCD for various treatment periods, and the amount of HVJ released into the culture medium was then estimated by a hemagglutinating activity assay. $^{**}P < 0.05$, $^{*}P < 0.01$ represent significant differences between the control group without MβCD treatment and the cholesterol-depleted cell group. The error bar represents the mean ± standard deviation

Structural and functional analysis of HVJ-CD

Electron microscopic analysis of both wild-type HVJ and HVJ-CD revealed envelope structures containing F protein (Fig. 3a). However, the cholesterol level of HVJ-CD was significantly lower than that of wild-type HVJ (Fig. 3b). As shown in Fig. 1d, the HA titer of HVJ-CD harvested from 15-cm dishes was measured and analyzed statistically; the HA titer of HVJ-CD was significantly higher than that of wild-type HVJ (Fig. 3c). However, when the titer was measured by HVJ-fusion activity, the titer of HVJ-CD was significantly lower than that of wild-type HVJ (Fig. 3d).

To investigate more precisely the characteristics of the HVJ-CD population, we then compared the sedimentation profiles of wild-type HVJ and HVJ-CD. Both HVJ populations in culture medium were fractionated on a linear sucrose gradient as described in the Materials and methods. Proteins in each sedimentation fraction were then subjected to SDS-PAGE analysis. Wild-type HVJ was mostly concentrated in two sedimentation fractions, corresponding to 30 and 35% sucrose (Fig. 4a). However, HVJ-CD was distributed over a wide range of fractions, from 15 to 60% sucrose (Fig. 4b). These results were confirmed by northern blotting of the HVJ genome in each fraction. While the wild-type HVJ genome was mainly detected between fractions 4 and 6 of the sucrose gradients, the HVJ-CD genome was detected in all of the fractions (Fig. 4a, b). Because these results suggested a variety in size and content of the HVJ-CD population, we examined HVJ-CD in each fraction by electron microscopy. The HVJ-CD particles were mainly present in fractions 2-8 and, in smaller amounts, in fractions 9-12, which tended to correlate with sucrose concentration. In fractions 11 and 12, both the genome and the proteins of HVJ-CD were detected, although no particles were detected by electron microscopy. In order to determine the distribution of soluble viral components after particle disruption, HVJ and HVJ-CD were treated with NP-40 [10], and the solubilized fraction was subjected to sucrose gradient centrifugation. HVJ components after NP-40 treatment were mainly detected in fraction 1 with approximately 15% in fraction 2 (Fig. 4e). Thus, the structure of HVJ-CD in fractions 11 and 12 was not clearly elucidated, but we concluded that typical particle structures were not present there. Smaller HVJ particles with a lower density accumulated in the lower-density fractions of the sucrose gradient and larger

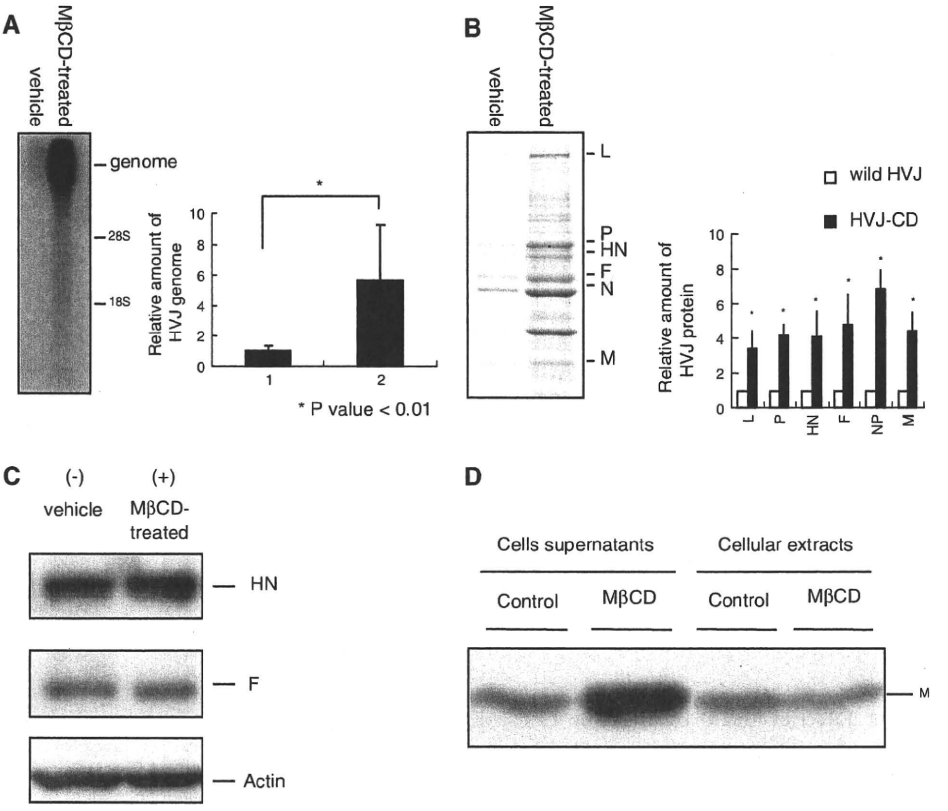

Fig. 2 Effects of cholesterol depletion on HVJ production. (**a**) Northern blot analysis of the HVJ genome produced by HVJ-infected LLC-MK2 cells. Quantification of the wild-type HVJ genome (lane 1) and the HVJ-CD genome (lane 2) is shown. The error bar represents the mean ± standard deviation. (**b**) SDS-PAGE analysis of wild-type HVJ (lane 1) and HVJ-CD (lane 2). Each HVJ protein was quantified by the intensity of each band. (**c**) Western blot analysis of HN and F proteins detected in HVJ-infected LLC-MK2 without (lane 1) or with (lane 2) MβCD treatment. (**d**) Western blot analysis of M protein in virus-like particles and LLC-MK2 cells producing virus-like particles, with or without MβCD treatment

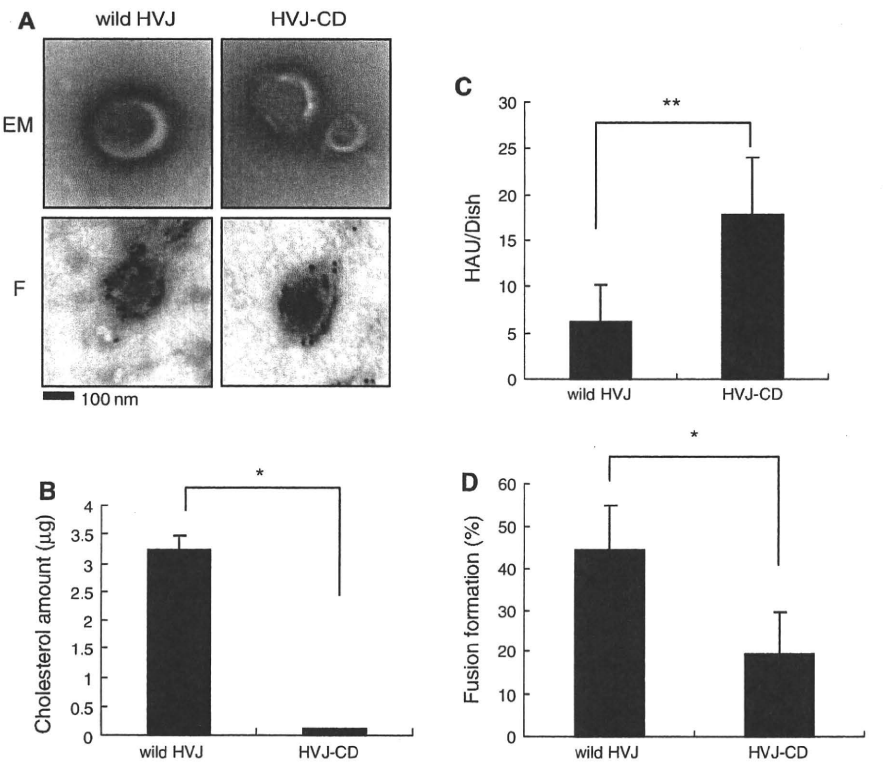

Fig. 3 Characterization of HVJ-CD morphology and infectivity. (**a**) Electron micrographs of wild-type HVJ (left panels) and HVJ-CD (right panels). Upper panels, transmission electron micrographs; lower panels, immunoelectron micrographs for F protein. (**b**) Quantification of envelope cholesterol in 2.4 HAU of wild-type HVJ and HVJ-CD. (**c**) HA assay of wild HVJ and HVJ-CD as described in Materials and methods. (**d**) The wild-type HVJ and HVJ-CD titers were measured by fusion activity. Fused cells were counted, and the proportion of fused cells in each field was calculated. $^{**}P < 0.05$, $^{*}P < 0.01$ represent significant differences between wild-type HVJ and HVJ-CD

HVJ particles were found in the higher-density fractions (Fig. 4c). We further compared the infectivity of HVJ-CD and wild-type HVJ in each fraction by detecting F protein expression in LLC-MK2 cells that had been inoculated with those fractions (Fig. 4d). Infectious particles of wild-type HVJ mainly accumulated in fractions 4-6. Conversely, none of the HVJ-CD-containing fractions showed significant infection of LLC-MK2 cells. Thus, membrane cholesterol depletion in infected cells induces production of HVJ with aberrant particle sizes and low infectivity.

The role of envelope cholesterol in HVJ infection

To evaluate the contribution of envelope cholesterol to HVJ infectivity, we examined the effect of cholesterol depletion from the HVJ envelope by direct treatment of wild-type HVJ with MβCD and measured the change in infectivity. HVJ was treated with 1% MβCD at 37°C for 6 h and then treated with 0.5 μg/ml of water-soluble cholesterol (Sigma Aldrich) at 37°C for 6 h. Cholesterol-depleted HVJ showed less than 5% of the original infectivity, as demonstrated by evaluating F protein expression in LLC-MK2 cells after infection (Fig. 5a, b, d). Subsequent incubation of the cholesterol-depleted HVJ with exogenous cholesterol solution did not restore infectivity (Fig. 5c, d), despite full recovery of the reduced membrane cholesterol (Fig. 5e). We then monitored the level of envelope proteins F and HN, both of which are indispensable for HVJ infection, during the course of depletion and recovery of envelope cholesterol. Western blot analysis did not show any evidence of a change in F and HN protein expression levels under the different envelope cholesterol conditions (Fig. 5f). These results suggest that cholesterol depletion causes an irreversible disruption. To investigate

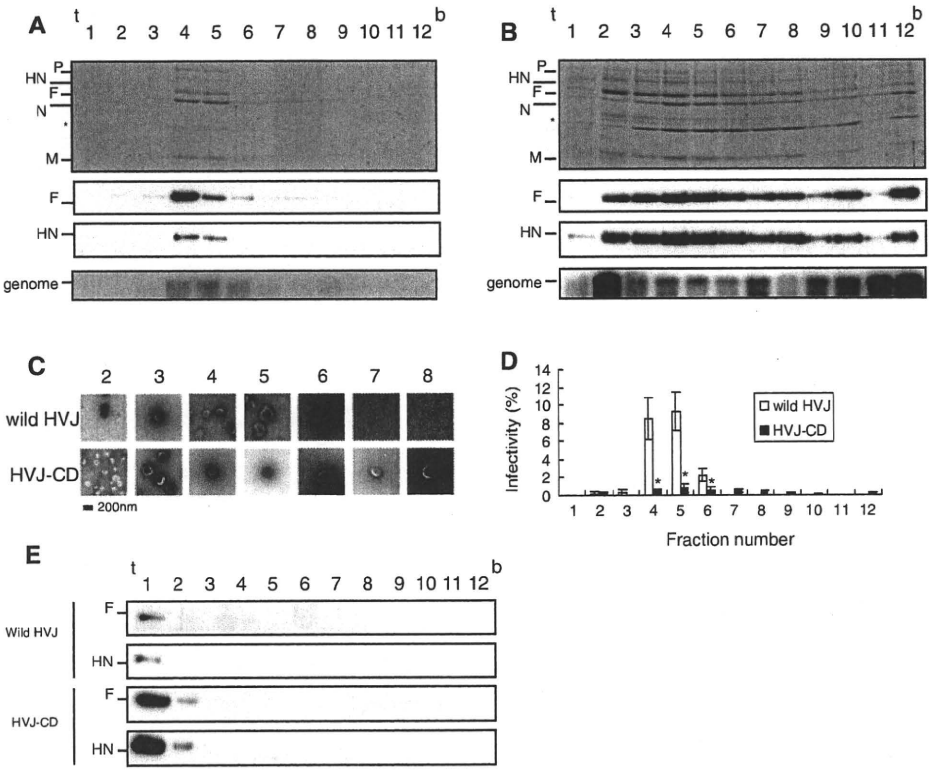

Fig. 4 Sucrose gradient analyses of HVJ produced by cholesterol-depleted LLC-MK2 cells and control LLC-MK2 cells. (**a**, **b**) Sucrose gradient fractionation of wild-type HVJ (**a**) and HVJ-CD (**b**). Upper panel, Coomassie brilliant blue staining of SDS-PAGE; upper middle panel, western blotting of F protein; lower middle panel, western blotting of HN protein; lower panel, northern blotting of the HVJ genome (t, top; b, bottom of sucrose gradient fractions). * : Actin, as previously reported [34]. (**c**) Transmission electron micrographs of fractions 2-8 of wild-type HVJ and HVJ-CD. (**d**) Expression of F protein from LLC-MK2 cells was visualized under 200-fold magnification by immunofluorescence microscopy. The infectivity of HVJ in each fraction was determined by the ratio of F protein-expressing LLC-MK2 cells in the total population after infection. (**e**) Sucrose gradient fractionation of NP40-treated wild HVJ and HVJ-CD. Upper panel, upper middle panel, western blotting of the F protein and the HN protein, respectively, of wild HVJ. Lower middle panel, lower panel, western blotting of the F protein and the HN protein, respectively, of HVJ-CD. The data represent the mean ± standard deviation (n=5). *$P < 0.01$ represents significant differences between wild-type HVJ and HVJ-CD